

Curved Nanomembrane-Based Concentric Ring Cavities for Supermode Hybridization

Jiawei Wang,^{†,‡,§,ID} Yin Yin,^{*,†,§,ID} Qi Hao,^{†,ID} Yue-De Yang,^{||} Sreeramu Valligatla,[†] Ehsan Saei Ghareh Naz,[†] Yuan Li,[†] Christian Niclaas Saggau,[†] Libo Ma,^{*,†,ID} and Oliver G. Schmidt^{†,‡}

[†]Institute for Integrative Nanosciences, IFW Dresden, Helmholtzstraße 20, 01069 Dresden, Germany

[‡]Material Systems for Nanoelectronics, Technische Universität Chemnitz, 09111 Chemnitz, Germany

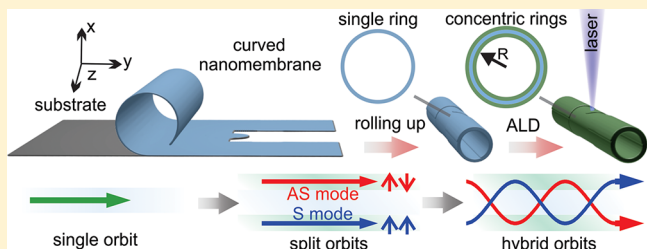
[§]Department of Physics, Xiamen University, Xiamen, 361005, China

^{||}State Key Laboratory of Integrated Optoelectronics, Institute of Semiconductors, Chinese Academy of Sciences, Beijing, 100083, China

Supporting Information

ABSTRACT: We report the mode interactions and resonant hybridization in nanomembrane-formed concentric dual ring cavities supporting whispering gallery mode resonances. Utilizing a rolled-up nanomembrane with subwavelength thickness as an interlayer, dual concentric microring cavities are formed by coating high-index nanomembranes on the inner and outer surfaces of the rolled-up dielectric nanomembrane. In such a hybrid cavity system, the conventional fundamental mode resonating along a single ring orbit splits into symmetric and antisymmetric modes confined by concentric dual ring orbits. Detuning of the coupled supermodes is realized by spatially resolved measurements along the cavity axial direction. A spectral anticrossing feature is observed as a clear evidence of strong coupling. Upon strong coupling, the resonant orbits of symmetric and antisymmetric modes cross over each other in the form of superwaves oscillating between the concentric rings with opposite phase. Notably, the present system provides high flexibilities in controlling the coupling strength by varying the thickness of the spacer layer and thus enables switching between strong and weak coupling regimes. Our work offers a compact and robust scheme using curved nanomembranes to realize novel cavity mode interactions for both fundamental and applied studies.

KEYWORDS: Curved nanomembrane, strong coupling, supermode, whispering gallery mode, mode splitting, hybrid orbits



Strong interactions of two eigenstates as a fundamental phenomenon exist in various physical systems such as localized plasmonic systems,¹ coupled atom-cavity systems,² exciton-polariton systems,^{3,4} acoustic cavities,⁵ optomechanical systems,⁶ and electromagnetic cavities.^{7,8} In photonics, the coupling between two or more optical eigenmodes leads to many nontrivial physical phenomena ranging from modifications of energy transfer,⁹ Fano resonances,¹⁰ electromagnetic-induced transparency,¹¹ slow light¹² to others in recently reported non-Hermitian photonic structures.^{10,13–15} Among these systems, optical microcavities especially those exhibiting whispering-gallery mode (WGM) resonances along a ring orbit have been identified as an ideal platform for studying those physical phenomena mentioned above.^{13–17} Putting two or more cavities into close proximity is a common strategy to study WGM coupling.^{18–23} In such a configuration, the optical coupling and energy transfer occur only at the tangent site of the neighboring cavities. Hence, optical coupling forms are limited by the intercavity configuration. In addition, the coupling gap is vulnerable to disturbance from mechanical vibrations or dust/nanoparticles contamination therein, which

might spoil the interactions substantially. Thus, it is of high interest to explore new schemes to manipulate the optical coupling behavior, which in consequence is expected to generate novel phenomena and applications.

In contrast to the outer-tangent configuration, concentric cavities provide an interesting configuration where optical coupling occurs along the whole concentric resonant orbits, and in turn, may lead to the formation of novel optical coupling behaviors. Previous studies have reported that WGMs can be supported in different layers in metal/dielectric-clad microcavities.^{24–28} However, establishing concentric dielectric ring structures with clearly defined coupling spacing and investigating the corresponding optical strong coupling behaviors have not been realized experimentally.

Here, we propose and demonstrate a novel scheme of mode coupling in concentric microcavities by depositing high-index dielectric layers onto both the outer and inner side of a low-

Received: August 25, 2018

Revised: October 10, 2018

Published: October 19, 2018

index nanomembrane-formed microtube cavity. In the initial microtube cavity, the WGM resonance is confined to the tubular-shaped low-index nanomembrane along a vertical ring orbit. After step-by-step deposition of high-index layers, the resonant orbit becomes split into the inner and outer concentric deposited layers, whereas the thin (~ 120 nm) low-index nanomembrane serves as a subwavelength spacing layer between the two concentric microring cavities. Because of the continuous variation of the effective cavity thickness along the tube axis, mode detuning is observed by spatially resolved mapping experiments. Spectral anticrossing is revealed as an evidence of strong coupling in the concentric microring cavities. In addition, switching between the strong and weak coupling regime is demonstrated by tailoring the winding number and coating thickness of the microtubular ring cavity. Numerical simulations of the mode detuning process are in good agreement with the experimental results.

Rolled-up nanotechnology enables mass-fabrication of nanomembrane-based optical microtube cavities which support WGM resonances.²⁹ Over more than one decade, rolled-up microtube cavities have been proven of great significance for fundamental studies of photon-plasmon coupling,³⁰ photonic molecules,³¹ spin-orbit coupling,³² and also practical applications such as optofluidic sensors,³³ broadband light sources³⁴ and on-chip integrated devices in the telecom band.³⁵ The well-controlled subwavelength wall thickness (~ 100 – 300 nm) is a unique and outstanding feature compared with other reported hollow-core WGM microcavities.^{36–38}

Figure 1a illustrates a microtube cavity prepared by rolling-up a prestrained $\text{SiO}_x/\text{SiO}_2$ nanomembrane (effective

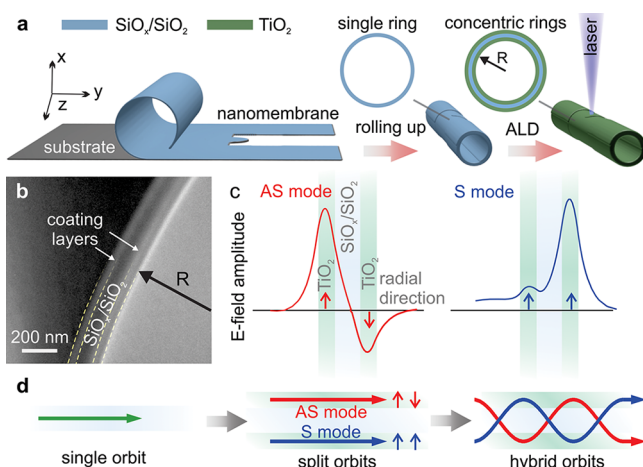


Figure 1. Schematics and images illustrating supermodes in concentric microcavities. (a) Schematic showing a rolled-up nanomembrane as the interlayer for the fabrication of concentric microcavities by ALD coating. (b) Concentric layer structure in the cross-section of fabricated microcavities is revealed by SEM measurement after cutting by focused ion beam. (c) Calculated electric field amplitude of S and AS modes with TM polarization. (d) Schematic showing the transition of resonant orbits from single ring to concentric rings.

refractive index $n_{\text{eff}} \sim 1.55$), where the resonant light is confined within the nanomembrane layer and the resonant orbit is along a single vertical ring in the rolled-up tube cavity.³⁹ Here, a parabolic-shaped lobe is introduced which provides axial optical confinement⁴⁰ and a varying winding

number W (i.e., varying thickness of the spacing layer) along the axial direction. By coating high-index TiO_2 layers ($n \sim 2.6$) on the inner and outer surfaces of the prepared microtube via atomic layer deposition (ALD), dual concentric microring cavities are formed owing to the presence of the high-index layers whereas the low index $\text{SiO}_x/\text{SiO}_2$ layer acts as the spacing layer, as shown in **Figure 1b**. As such, the intercavity coupling gap is accurately determined by the subwavelength thin nanomembrane with rigid mechanical stability. Light fields in the two high-index layers with a large spatial overlapping facilitate the mutual interactions.

A pair of split modes (also termed as “supermodes”¹⁸) delocalized in the two coupled concentric cavities are revealed by numerical calculations for transverse-magnetic (TM, electric fields parallel to the tube axis) polarized light in the optical regime, as shown in **Figure 1c**. In the neighboring dual cavities, the resonant mode splits into symmetric (S) and antisymmetric (AS) modes. The S mode consists of parallel field vectors of the oscillating optical field distributed in the inner and outer ring cavities while the AS mode comprises antiparallel vectors of the oscillating field in all of the concentric resonant orbits. Compared to chemical molecular systems, the mode hybridization in our coupled photonic system (also known as a photonic molecule¹⁸) is an optical analogue of split electron energy levels in highest occupied molecular orbital (HOMO) and lowest unoccupied molecular orbital (LUMO) where the electron spin vectors in the molecular orbitals are parallel and antiparallel, respectively. By mode detuning, strong coupling between S and AS modes occurs and strongly “hybridized” resonant orbits cross over each other in the concentric rings, as shown in **Figure 1d**.

For experiments, $\text{SiO}_x/\text{SiO}_2$ microtube cavities with radii $R \sim 6.5 \mu\text{m}$ are fabricated via rolled-up nanotechnology (see **Methods**).⁴¹ A 60 nm thick nanomembrane was rolled up for ~ 2 windings, resulting in a cavity wall thickness of ~ 120 nm. We characterize the resonant light emission from microtubes using a microphotoluminescence (μPL) measurement setup (see **Methods**). Optical resonances are built up by PL emission originating from defects in the amorphous silica with energies ranging from ~ 1.5 to ~ 2.5 eV. The high-index TiO_2 layer was coated by ALD step-by-step and the corresponding resonant spectra are summarized in **Figure 2a**. For a bare microtube without ALD coating, the designed lobe structure in the middle leads to an optical quasi-potential well and hence the formation of multiple axial modes.^{32,40} Upon a thick high-index layer coating, the axial modes are suppressed, which is caused by the weakened contrast of average refractive index between the lobe region and its vicinity. When the coating layer is up to ~ 60 nm thick, the original fundamental mode splits into two modes while high-order axial modes completely disappear. Meanwhile the averaged quality (Q) factor of TM mode experiences a significant degradation, which is mainly attributed to the suppressed axial confinement for both split S and AS modes (see **Supporting Information Section I**).

One should note that this kind of split modes are different from the previously reported higher order radial modes.⁴² **Figure 2b** shows the mode energies as a function of mode serial number Δm (with the baseline of mode series labeled in **Figure 2a**), which reveals clearly two sets of modes with respective mode spacing and n_{eff} . Typically, AS modes suggest a lower Q factor compared with that of S modes because of a larger notch-induced scattering loss of the localized mode profile.^{43,44} This serves as a characteristic feature for distinguishing

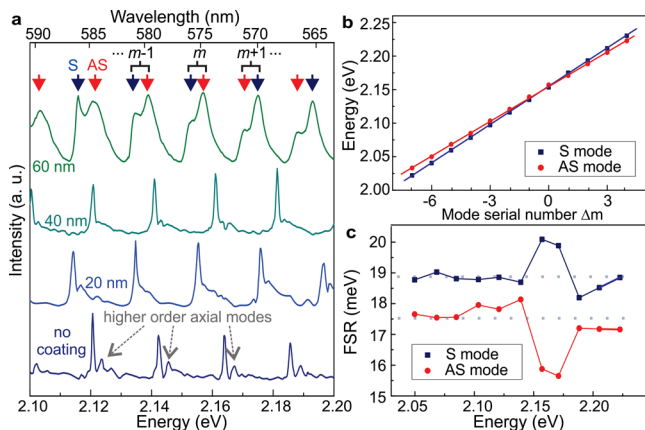


Figure 2. Evolution of resonant modes upon increased coating layer thickness. (a) Measured resonant spectra upon coating thickness of 0, 20, 40, and 60 nm. (b) Extracted mode energies as a function of Δm upon 60 nm thick coating. Solid lines are linear fits. (c) Extracted FSR as a function of mode energy upon 60 nm-thick coating. Gray dashed line indicates the averaged FSR through a linear fit.

between the mode pairs. In Figure 2c, one can also distinguish the AS and S modes by the $\sim 10\%$ difference in free spectral range (FSRs) due to the different n_{eff} for two modes. The AS mode with a smaller FSR suggests a higher n_{eff} than that of the S mode due to less field overlapping in the spacing layer and a larger portion confined inside the high-index layers. Notably, the approach of the S and AS modes is observed at a mode energy of around 2.16 eV. Similarly, significant fluctuations of the FSR for S and AS modes are revealed at ~ 2.16 eV position, too, as a signature of strong optical coupling. In contrast, for transverse-electric (TE, electric fields perpendicular to the tube axis) polarization, no mode splitting is observed for coating layers up to 60 nm thick due to a “slot-mode”-like profile with strong overlap in the middle low-index region⁴⁵ (see characterization and simulation results in Supporting Information Section I).

To better visualize the mode splitting and hybridization, we carried out two-dimensional (2D) numerical simulations using the finite-element method (COMSOL Wave Optics Module). The cross-sectional view of a rolled-up tube is described as a spiral shape with an outermost radius of $\sim 4 \mu\text{m}$ (limited by the computation power).⁴¹ Figure 3a presents the simulated resonant spectra upon varying the coating thickness from 0 to 80 nm. One can discern mode splitting with coating thickness larger than 40 nm. In experiments, the emerging AS modes at ~ 40 nm-thick coating may be too weak for detection. In insets i and ii, clear WGM profiles can be identified in a cross-sectional view of the microtube cavity. The S mode suggests a strong overlapping in the outer cavity but also a significant portion in the low-index spacing layer (see inset i). In contrast, for the AS mode, most of the field is localized in the inner cavity orbit while the field staying in the spacing layer is much weaker than that of the S mode (see inset ii). Similar to the experimental observation in Figure 2b,c, two sets of modes with $\sim 14\%$ differences of FSRs are presented (see Figure 3b,c). Modulation of FSRs at ~ 2.20 eV for both modes is also discerned due to the repelling of mode energies upon strong coupling.¹³

The coupling strength between S and AS modes can be examined by spectral detuning and studying the evolution of the hybridized modes. One common approach is to employ localized heating on one cavity to tune its n_{eff} .¹⁹ Instead of thermal heating, in our unique concentric dual rings based on rolled-up microtube cavities, the coupling strength can be tuned by changing the average thickness of the spacing layer. As shown in Figure 4a, the designed lobe-modified tube naturally provides a continuously varying W (i.e., equivalently the average thickness of the cavity wall) along the tube axis. Thus, we can utilize the axial dimension of the tube cavity as a new degree of freedom to investigate the evolution of optical coupling between the split AS and S modes.

As shown in Figure 4b, spatially resolved measurements are performed by scanning along the tube axis from $z = 0$ (lobe center) to $10 \mu\text{m}$, which corresponding to a decreased W from ~ 2.5 to ~ 2.25 . A slightly decreased W of the nanomembrane-

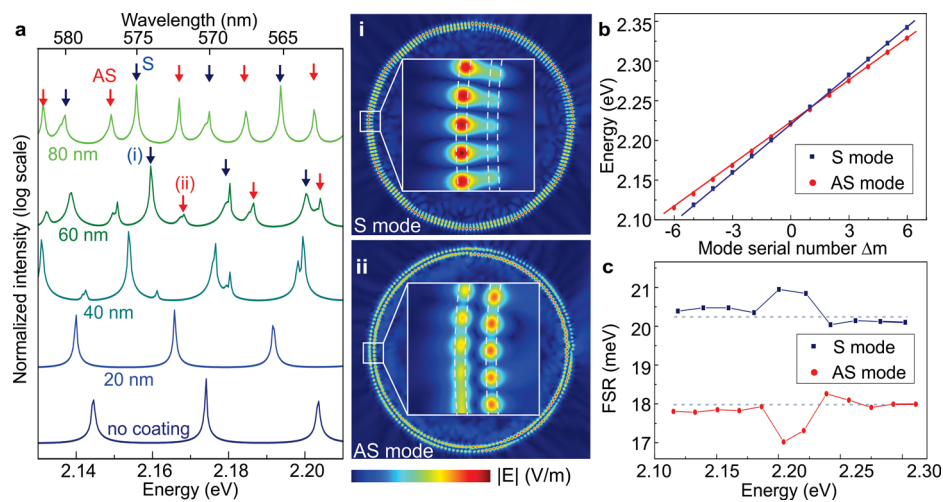


Figure 3. Simulated resonant modes with increasing coating thickness. (a) Simulated TM mode resonant spectra upon varying coating thickness from 0 to 80 nm. Insets: Simulated electric field intensity distributions in a cross-sectional view for (i) S mode; (ii) AS mode. (b) Extracted mode energies as a function of Δm for 60 nm thick coating. Solid lines are linear fits. (c) Extracted FSR as a function of mode energy upon 60 nm thick coating. Gray dashed line indicates the averaged FSR through a linear fit.

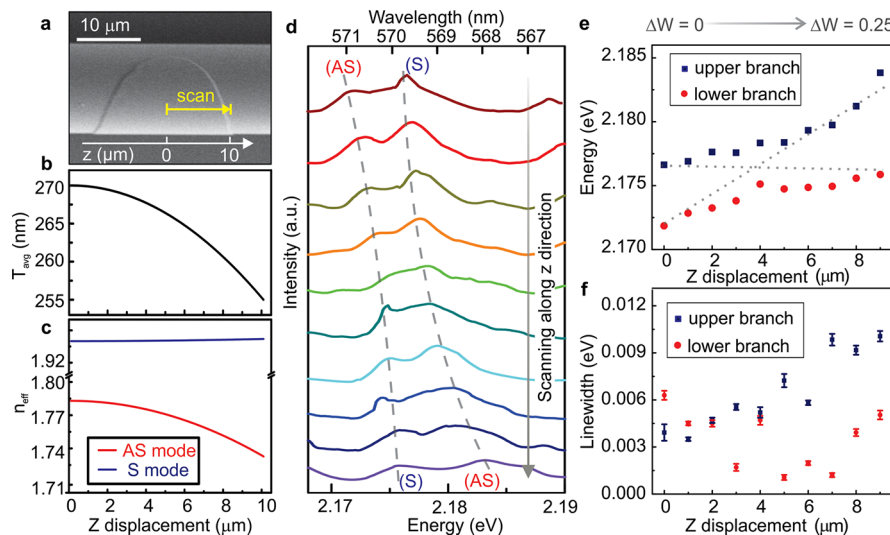


Figure 4. Detuning of supermodes by spatially resolved measurements along the axial direction. (a) SEM image of concentric cavities around the lobe region illustrating measurements at positions with varying W from ~ 2.5 to ~ 2.25 . (b) Calculated averaged thickness T_{avg} as a function of axial displacement. (c) Calculated n_{eff} for both split modes as a function of axial displacement. (d) Resonant spectra measured at shifted axial positions. (e) Extracted mode energy as a function of axial displacement. (f) Extracted mode linewidth as a function of axial displacement. Mode energies and linewidths are extracted by fitting the spectrum with two Lorentzian curves.

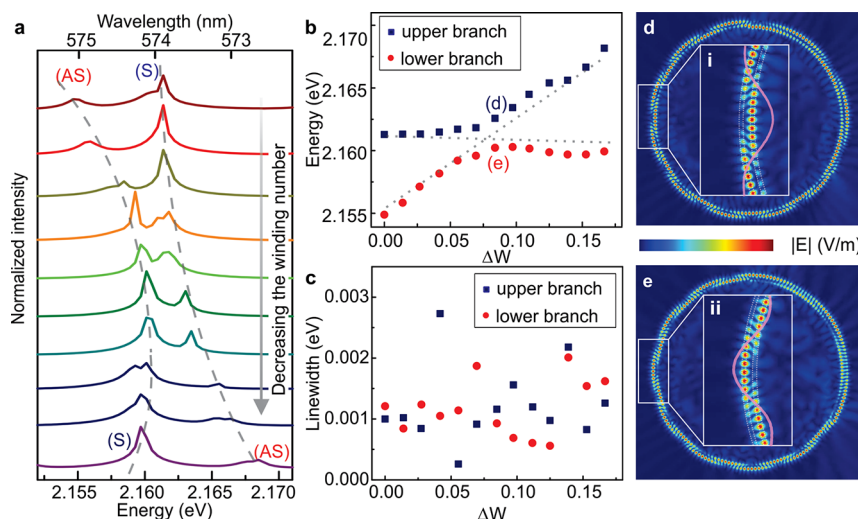


Figure 5. Simulated detuning of supermodes upon a decreased winding number. (a) Simulated resonant spectra measured with varying W from 2.5 to 2.33. (b) Extracted mode energy as a function of ΔW . (c) Extracted mode linewidth as a function of ΔW . (d)-(e) Simulated mode field distributions in strong coupling regime showing the hybrid orbits of two supermodes. Insets: Zoom-in views of (d,e) show waveforms of the superwaves oscillating between the concentric microrings with opposite phase.

based spacing layer leads to distinctive perturbations of n_{eff} and thus mode shifts of the two coupled modes. Numerical simulation results reveal that a strong modulation of the AS mode is expected while that of the S mode is much less prominent. The calculation is nicely verified by a control experiment (see Supporting Information Section II) for two independently tuned modes without efficient coupling, which indicates a strong spectral tuning effect of the AS mode while the spectral shift of the S mode is negligible.

Figure 4d shows the variation of the resonant spectra of the AS and S modes when mapping along the tube axis in the lobe region. While the AS mode is spectrally detuned across the S mode, the spacing of the coupled modes first decreases from 8.0 to 3.1 meV at a Z offset of $\sim 4 \mu\text{m}$, and then increases to 4.8 meV at $Z \sim 10 \mu\text{m}$, as shown in Figure 4e. This trend agrees with the anticrossing feature observed in conventional two-

element photonic molecules and confirms the strong coupling behavior. Figure 4f summarizes the change of linewidths over the detuning process. Because of the rolling-up induced spiral shape for both inner and outer cavities, a specified mode is strongly scattered by the lobes (i.e., rolling ends) depending on their azimuthal positions.⁴⁶ In the mapping measurement along the tube axis, the azimuthal position of the outer lobe gradually changes, which leads to varying scattering loss for a given resonant mode and hence causes additional changes to the mode linewidth. Nevertheless, here a crossing trend of linewidths can be identified in two branches, showing a minimum value difference (~ 0.6 meV) at Z offset of $\sim 4 \mu\text{m}$, which is also a sign of energy transfer under strong mode hybridization.¹³

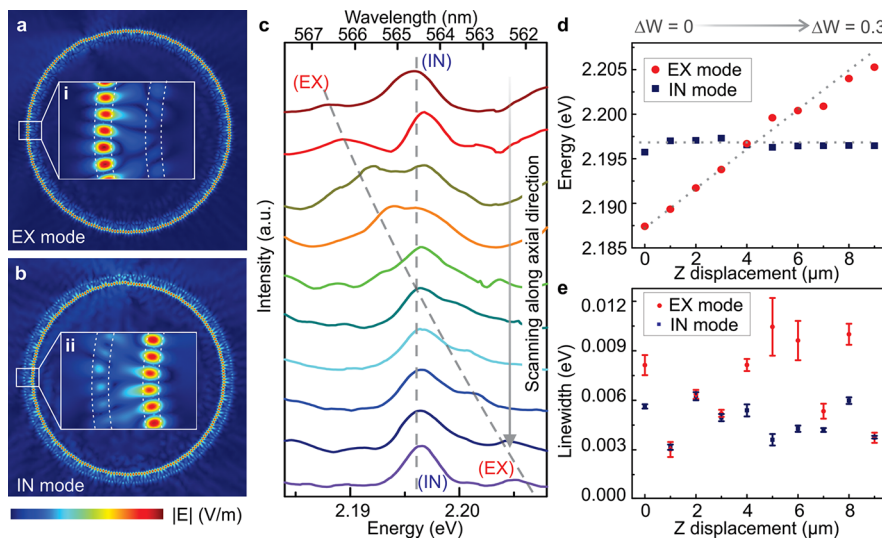


Figure 6. Detuning of split modes in the weak coupling regime. (a,b) Simulated mode field intensity distributions of (a) EX mode and (b) IN mode. Insets: Zoom-in views of (a,b). (c) Resonant spectra measured at different axial positions. (d) Extracted mode energy as a function of axial displacement. (e) Extracted mode linewidth as a function of axial displacement.

The mode coupling in such an open system can be generally described using a 2×2 non-Hermitian Hamiltonian matrix¹³ as follows

$$H = \begin{bmatrix} E_1 - i\gamma_1 & V_1 \\ V_2 & E_2 - i\gamma_2 \end{bmatrix} \quad (1)$$

where E_1 and E_2 are the original eigenenergies, and γ_1 and γ_2 are the decay rates. V_1 and V_2 are the coupling terms. The newly formed eigenstates can be expressed as

$$E_{\pm} = E_+ - i\gamma_+ \pm \sqrt{(E_- - i\gamma_-)^2 + V_1 V_2} \quad (2)$$

where $E_{\pm} = (E_1 \pm E_2)/2$ and $\gamma_{\pm} = (\gamma_1 \pm \gamma_2)/2$. The anticrossing feature confirms the strong coupling criteria ($|V_1 V_2| > |\gamma_-|^2$). On the basis of the statistical results of differential decay rates ($|\gamma_-| \sim 0.9 \pm 0.4$ meV, see Supporting Information Section III), the coupling strength is estimated as ~1.9 meV.

Figure 5a shows the simulated resonant spectra with varying winding number W from 2.5 to 2.33. The AS mode is tuned continuously across the S mode, which agrees very well with the experimental results. Figure 5b indicates that the mode spacing first shrinks from 6.4 to 2.0 meV, and continuously increases to 8.3 meV, which confirms the strong coupling behavior in the simulated concentric cavities. Besides, a crossing trend of linewidths is revealed in Figure 5c at $\Delta W \sim 0.085$ with a minimum discernible difference ~0.3 meV. Figure 5d,e presents the simulated mode field distributions at the strong coupling regime. Instead of a dominant distribution in the inner(outer) ring for the AS(S) mode, the intensity of coupled supermodes hop between the inner and outer ring orbits in the oscillating form with opposite phase. The energy transfer is enabled upon such orbits that cross over each other, which is not revealed from previous reports. These oscillating hopping waves assume a novel type of WGM resonance along the concentric dual rings. Owing to the orthogonally distributed AS and S modes in the hopping waveforms, the AS(S) mode periodically appears at the outer ring where the AS(S) mode can be coupled to the surrounding device while the other S(AS) mode is suppressed to be coupled out. This

behavior may lead to some interesting applications such as angle-resolved coupling of hybrid modes in a compact photonic molecule.

The unique way of constructing such a concentric cavity system enables a flexible control over the coupling strength by tailoring the thickness of the spacing and ALD coating layers. Upon a thicker spacing layer, split modes, termed as inner (IN) and exterior (EX) modes, become separately localized in the inner and outer ring cavities (see Figure 6a,b) instead of strongly coupled S and AS modes (see Supporting Information Section III).

To verify the switching effect between strongly and weakly coupled regime, a tube cavity with thicker spacing and coating layer is characterized, where $W \sim 4.2$ and the ALD thickness is 100 nm. Figure 6c shows the mode detuning process by varying W from 4.2 to 3.9. The EX mode gradually blueshifts due to the decreased n_{eff} while no apparent spectral shift is present for the IN mode. As shown in Figure 6d, the mode spacing first shrinks from 8.8 to 0.1 meV and increases again to 8.3 meV, which suggests that the spectral anticrossing no longer exists under the weak coupling condition. In Figure 6e, the differential linewidth of ~2.8 meV at the crossing point of eigenenergies is much larger than the values for strong coupling and implies a noncrossing feature. The weak coupling behavior is examined by numerical simulations (see Supporting Information Section III). The crossing point in the mode energy suggests a significant differential linewidth of ~2.6 meV, which agrees with the experimental observation and reveals the feature of weak coupling.

In addition to the adopted approach for mode detuning, other alternative ways are also feasible. The rolled-up microtubes have been demonstrated with the capability of liquid solution delivery inside the hollow-core tubular structure for optofluidic sensing.⁴⁷ This can be potentially useful to detune the split modes and examine the spectral anticrossing behavior. Besides, a step-by-step change of the inner-coating layer thickness (e.g., injection of a solution containing biomaterials to form a homogeneous coating onto the inner layer) potentially leads to a distinctive perturbation of the two modes (see Supporting Information Section IV). The potential

modulation effect caused by varying lobe positions in our scheme can be mitigated so that the evolution of mode linewidth due to intercavity coupling can be better revealed. Simulation results suggest crossing of the linewidth upon strong coupling and avoided crossing upon weak coupling, which is in good agreement with previous two-cavity coupling systems in the case of internal coupling.⁴⁸ This is in contrast to results for external coupling of dual microcavities where a splitting to one high-Q and one low-Q mode is expected.^{49–51} Besides, independent tuning of the absorption loss of inner/outer layer (e.g., by a metal-coated probe with strong absorption) can serve as an additional control knob for studying such a non-Hermitian system in the future.¹⁴

In summary, we have proposed and demonstrated a strategy to study mode interactions in concentric microring cavities where the coupling gap is defined by a subwavelength spacing nanomembrane. The rolled-up nanomembranes naturally serve as a nice skeleton for fabricating the concentric WGM cavities via ALD. The experimental results suggest a transition from a single resonant orbit to two split orbits in the radial direction, namely S and AS modes. Axial mapping measurements have been carried out to reveal spectral anticrossing behavior in the strong coupling regime. More interestingly, the resonant orbits of AS and S modes cross over each other in the concentric rings in a form of oscillating waveforms, which results in azimuthal angle-dependent field distributions for AS and S modes. Besides, switching between the strong and weak coupling regime was demonstrated by tailoring the thickness of the spacing and coating layers. One should note that the optical resonances are enabled by coupling laser-excited PL emission into the microtube cavity. It will be highly interesting to characterize optical transmission with angle-selective coupling of hybridized modes through a tunable laser excitation. However, one should notice that the current free-space coupling configuration may lead to a low coupling efficiency whereas a near-field coupling scheme (e.g., a tapered fiber) is preferred.⁵² We envision that the rolled-up microtube-based concentric cavities will serve as a novel platform for future fundamental studies such as Non-Hermitian physics and realization of the exceptional point (EP). Moreover, due to the different sensitivities of split modes to external perturbations or energy injections, this system could be also highly promising for practical applications such as self-referenced sensors²⁴ (especially with operation around EP for ultrasensitive detection¹⁷) or dual-ring-based single mode lasers with broken PT-symmetry.¹⁵

Methods. *Fabrication of Concentric Cavities.* The nanomembrane-based optical microtube cavities were fabricated with the process flow modified based on our previous work.⁴¹ A 2 μm thick photoresist layer (ARP-3510, Allresists GmbH) was first patterned on a silicon substrate with a 1 μm thick thermal oxide layer by a maskless lithography process (μPG 101, Heidelberg Instruments). In order to obtain a reasonably high Q factor, a U-shape pattern is adopted which allows the middle part of the tube to be free-standing after rolling-up and largely suppresses the substrate leakage loss.

Differentially strained 20 nm SiO and 40 nm SiO₂ layers were deposited by angled electron-beam deposition (Edwards Auto500 e-beam) at a glancing angle of 60°. The difference of deposition rate from 5 Å/s (SiO) to 0.5 Å/s (SiO₂) leads to differentially strained layers for rolling. Rolling occurred when the photoresist layer was dissolved in dimethyl sulfoxide (DMSO). A critical point dryer (931 GL, Tousimis CPD) was

employed to avoid the structure change during the evaporation of solvents. TiO₂ film was coated on the inner and outer wall of the microtube using atomic layer deposition (FlexAL, Oxford Instruments). Tetrakis(dimethylamino)titanium (TDMAT) and O₂ were used as precursors at a substrate temperature of 150 °C. The estimated deposition rate is ~0.3 Å /cycle.

Spatially and Energetically Resolved Characterizations. The PL spectra of microtube cavities were measured using a microphotoluminescence laser confocal setup (LabRAM HR Evolution, HORIBA Scientific). An excitation laser beam at 457 nm was focused onto the tube top surface using a 50× long working distance objective lens with a spot size ~0.9 μm². Such a focused laser beam allows us to perform spatially resolved measurements with a resolution of 1 μm. The laser power onto the sample was adjusted to ~0.2 mW. The emission signal was collected by the same objective lens and analyzed by a spectrometer with 600 blz/mm. The polarization state of the emission light was determined using a rotatable half-wave plate and a fixed polarization analyzer. The microtube sample was mounted on a motorized stage for spatial-selective optical excitation.

■ ASSOCIATED CONTENT

§ Supporting Information

The Supporting Information is available free of charge on the ACS Publications website at DOI: [10.1021/acs.nanolett.8b03453](https://doi.org/10.1021/acs.nanolett.8b03453).

Characterizations upon TE polarization in concentric microring cavities (Section I, Figure S1–S3); control experiment of mode detuning upon varying winding number (Section II, Figure S4); simulation of split modes in the weak coupling regime (Section III, Figure S5); evolution of mode linewidths upon strong and weak coupling (section IV, Figure S6) ([PDF](#))

■ AUTHOR INFORMATION

Corresponding Authors

*(L.M.) E-mail: l.ma@ifw-dresden.de. Tel.: +49 (0) 351 4659 1153. Fax: +49 (0) 351 4659 782.

*(Y.Y.) E-mail: y.yin@outlook.com. Tel.: +49 (0) 351 4659 1153. Fax: +49 (0) 351 4659 782.

ORCID ®

Jiawei Wang: [0000-0001-6323-8081](https://orcid.org/0000-0001-6323-8081)

Yin Yin: [0000-0002-5318-0020](https://orcid.org/0000-0002-5318-0020)

Qi Hao: [0000-0002-5525-4417](https://orcid.org/0000-0002-5525-4417)

Libo Ma: [0000-0001-9850-2292](https://orcid.org/0000-0001-9850-2292)

Author Contributions

L.M., J.W., and O.G.S. conceived the concept of concentric cavities. J.W., Q.H., and S.V. fabricated the concentric cavities. J.W., Y.Y., and E.S. performed the experiments. J.W., Y.Y., and Y.-D.Y. performed numerical simulations. Y.L. and C.N.S. helped with sample characterizations. J.W. and L.M. wrote the manuscript with contributions from all authors.

Notes

The authors declare no competing financial interest.

■ ACKNOWLEDGMENTS

The authors thank R. Engelhard, S. Baunack, and L. Schröder for technical support. This work was supported by the German Research Foundation DFG (Grant FOR 1713, SCHM 1298/22-1 and Leibniz program).

■ REFERENCES

- (1) Lourenço-Martins, H.; Das, P.; Tizei, L. H.; Weil, R.; Kociak, M. *Nat. Phys.* **2018**, *14*, 360.
- (2) Choi, Y.; Kang, S.; Lim, S.; Kim, W.; Kim, J.-R.; Lee, J.-H.; An, K. *Phys. Rev. Lett.* **2010**, *104*, 153601.
- (3) Liu, X.; Galfsky, T.; Sun, Z.; Xia, F.; Lin, E.-c.; Lee, Y.-H.; Kéna-Cohen, S.; Menon, V. M. *Nat. Photonics* **2015**, *9*, 30.
- (4) Gong, S.-H.; Ko, S.-M.; Jang, M.-H.; Cho, Y.-H. *Nano Lett.* **2015**, *15*, 4517–4524.
- (5) Ding, K.; Ma, G.; Xiao, M.; Zhang, Z.; Chan, C. T. *Phys. Rev. X* **2016**, *6*, No. 021007.
- (6) Gröblacher, S.; Hammerer, K.; Vanner, M. R.; Aspelmeyer, M. *Nature* **2009**, *460*, 724.
- (7) Lee, S.-B.; Yang, J.; Moon, S.; Lee, S.-Y.; Shim, J.-B.; Kim, S. W.; Lee, J.-H.; An, K. *Phys. Rev. Lett.* **2009**, *103*, 134101.
- (8) Shin, Y.; Kwak, H.; Moon, S.; Lee, S.-B.; Yang, J.; An, K. *Sci. Rep.* **2016**, *6*, 38826.
- (9) Coles, D. M.; Yang, Y.; Wang, Y.; Grant, R. T.; Taylor, R. A.; Saikin, S. K.; Aspuru-Guzik, A.; Lidzey, D. G.; Tang, J. K.-H.; Smith, J. M. *Nat. Commun.* **2014**, *5*, 5561.
- (10) Limonov, M. F.; Rybin, M. V.; Poddubny, A. N.; Kivshar, Y. S. *Nat. Photonics* **2017**, *11*, 543.
- (11) Peng, B.; Özdemir, S. K.; Chen, W.; Nori, F.; Yang, L. *Nat. Commun.* **2014**, *5*, 5082.
- (12) Xia, F.; Sekaric, L.; Vlasov, Y. *Nat. Photonics* **2007**, *1*, 65.
- (13) Cao, H.; Wiersig, J. *Rev. Mod. Phys.* **2015**, *87*, 61.
- (14) Peng, B.; Özdemir, S.; Rotter, S.; Yilmaz, H.; Liertzer, M.; Monifi, F.; Bender, C.; Nori, F.; Yang, L. *Science* **2014**, *346*, 328–332.
- (15) Hodaei, H.; Miri, M.-A.; Heinrich, M.; Christodoulides, D. N.; Khajavikhan, M. *Science* **2014**, *346*, 975–978.
- (16) Xiao, Y.-F.; Liu, Y.-C.; Li, B.-B.; Chen, Y.-L.; Li, Y.; Gong, Q. *Phys. Rev. A: At., Mol., Opt. Phys.* **2012**, *85*, No. 031805.
- (17) Chen, W.; Özdemir, S. K.; Zhao, G.; Wiersig, J.; Yang, L. *Nature* **2017**, *548*, 192.
- (18) Peng, B.; Özdemir, S. K.; Zhu, J.; Yang, L. *Opt. Lett.* **2012**, *37*, 3435–3437.
- (19) Benyoucef, M.; Kiravittaya, S.; Mei, Y.; Rastelli, A.; Schmidt, O. G. *Phys. Rev. B: Condens. Matter Mater. Phys.* **2008**, *77*, 035108.
- (20) Grossmann, T.; Wienhold, T.; Bog, U.; Beck, T.; Friedmann, C.; Kalt, H.; Mappes, T. *Light: Sci. Appl.* **2013**, *2*, e82.
- (21) Du, H.; Zhang, X.; Chen, G.; Deng, J.; Chau, F. S.; Zhou, G. *Sci. Rep.* **2016**, *6*, 24766.
- (22) Schmidt, C.; Liebsch, M.; Klein, A.; Janunts, N.; Chipouline, A.; Käsebier, T.; Etrich, C.; Lederer, F.; Kley, E.-B.; Tünnermann, A. *Phys. Rev. A: At., Mol., Opt. Phys.* **2012**, *85*, 033827.
- (23) Zhao, J.; Yan, Y.; Wei, C.; Zhang, W.; Gao, Z.; Zhao, Y. S. *Nano Lett.* **2018**, *18*, 1241–1245.
- (24) Ling, T.; Guo, L. J. *Appl. Phys. Lett.* **2013**, *103*, 013702.
- (25) Teraoka, I.; Arnold, S. *Opt. Lett.* **2007**, *32*, 1147–1149.
- (26) Xiao, Y.-F.; Zou, C.-L.; Li, B.-B.; Li, Y.; Dong, C.-H.; Han, Z.-F.; Gong, Q. *Phys. Rev. Lett.* **2010**, *105*, 153902.
- (27) Cai, S.; Xiang, Y.; Miao, Y.; Li, M.; Peng, Y.; Song, Y. *Opt. Express* **2016**, *24*, 13832–13838.
- (28) Lu, Q.; Li, M.; Liao, J.; Liu, S.; Wu, X.; Liu, L.; Xu, L. *Opt. Lett.* **2015**, *40*, 5842–5845.
- (29) Li, X. *Adv. Opt. Photonics* **2011**, *3*, 366–387.
- (30) Yin, Y.; Wang, J.; Lu, X.; Hao, Q.; Saei Ghareh Naz, E.; Cheng, C.; Ma, L.; Schmidt, O. G. *ACS Nano* **2018**, *12*, 3726–3732.
- (31) Wang, J.; Yin, Y.; Hao, Q.; Zhang, Y.; Ma, L.; Schmidt, O. G. *Adv. Opt. Mater.* **2018**, *6*, 6.
- (32) Ma, L.; Li, S.; Fomin, V.; Hentschel, M.; Götte, J.; Yin, Y.; Jorgensen, M.; Schmidt, O. G. *Nat. Commun.* **2016**, *7*, 10983.
- (33) Madani, A.; Harazim, S. M.; Quiñones, V. A. B.; Kleinert, M.; Finn, A.; Naz, E. S. G.; Ma, L.; Schmidt, O. G. *Opt. Lett.* **2017**, *42*, 486–489.
- (34) Li, F.; Mi, Z. *Opt. Express* **2009**, *17*, 19933–19939.
- (35) Yu, X.; Goddard, L. L.; Zhu, J.; Li, X.; Chen, X. *Appl. Phys. Lett.* **2018**, *112*, 021108.
- (36) Rakovich, Y. P.; Balakrishnan, S.; Donegan, J. F.; Perova, T. S.; Moore, R. A.; Gun'ko, Y. K. *Adv. Funct. Mater.* **2007**, *17*, 1106–1114.
- (37) Zhan, J.; Dong, H.; Sun, S.; Ren, X.; Liu, J.; Chen, Z.; Lienau, C.; Zhang, L. *Adv. Opt. Mater.* **2016**, *4*, 126–134.
- (38) Kim, K. H.; Fan, X. *Appl. Phys. Lett.* **2014**, *105*, 191101.
- (39) Ma, L.; Li, S.; Quiñones, V. A. B.; Yang, L.; Xi, W.; Jorgensen, M.; Baunack, S.; Mei, Y.; Kiravittaya, S.; Schmidt, O. G. *Adv. Mater.* **2013**, *25*, 2357–2361.
- (40) Strelow, C.; Rehberg, H.; Schultz, C.; Welsch, H.; Heyn, C.; Heitmann, D.; Kipp, T. *Phys. Rev. Lett.* **2008**, *101*, 127403.
- (41) Wang, J.; Yin, Y.; Hao, Q.; Huang, S.; Saei Ghareh Naz, E.; Schmidt, O. G.; Ma, L. *ACS Photonics* **2018**, *5*, 2060–2067.
- (42) Trommer, J.; Böttner, S.; Li, S.; Kiravittaya, S.; Jorgensen, M. R.; Schmidt, O. G. *Opt. Lett.* **2014**, *39*, 6335–6338.
- (43) Böttner, S.; Li, S.; Trommer, J.; Kiravittaya, S.; Schmidt, O. G. *Opt. Lett.* **2012**, *37*, 5136–5138.
- (44) Jiang, X. F.; Zou, C. L.; Wang, L.; Gong, Q.; Xiao, Y. F. *Laser Photonics Rev.* **2016**, *10*, 40–61.
- (45) Almeida, V. R.; Xu, Q.; Barrios, C. A.; Lipson, M. *Opt. Lett.* **2004**, *29*, 1209–1211.
- (46) Fang, Y.; Li, S.; Mei, Y. *Phys. Rev. A: At., Mol., Opt. Phys.* **2016**, *94*, 033804.
- (47) Harazim, S. M.; Quiñones, V. A. B.; Kiravittaya, S.; Sanchez, S.; Schmidt, O. G. *Lab Chip* **2012**, *12*, 2649–2655.
- (48) Boriskina, S. V. *Opt. Lett.* **2007**, *32*, 1557–1559.
- (49) Atlasov, K. A.; Karlsson, K. F.; Rudra, A.; Dwir, B.; Kapon, E. *Opt. Express* **2008**, *16*, 16255–16264.
- (50) Benyoucef, M.; Shim, J.-B.; Wiersig, J.; Schmidt, O. G. *Opt. Lett.* **2011**, *36*, 1317–1319.
- (51) Song, Q.; Cao, H. *Phys. Rev. Lett.* **2010**, *105*, 053902.
- (52) Jiang, X.; Shao, L.; Zhang, S.-X.; Yi, X.; Wiersig, J.; Wang, L.; Gong, Q.; Lončar, M.; Yang, L.; Xiao, Y.-F. *Science* **2017**, *358*, 344–347.